🔓**Open Access**

Fast Single-Image Dehazing Algorithm Based on Piecewise Transformation in Optical Model

Guoling Bi
Lirong Wang
Changzheng Chen
Xingxiang Zhang
Guoning Li
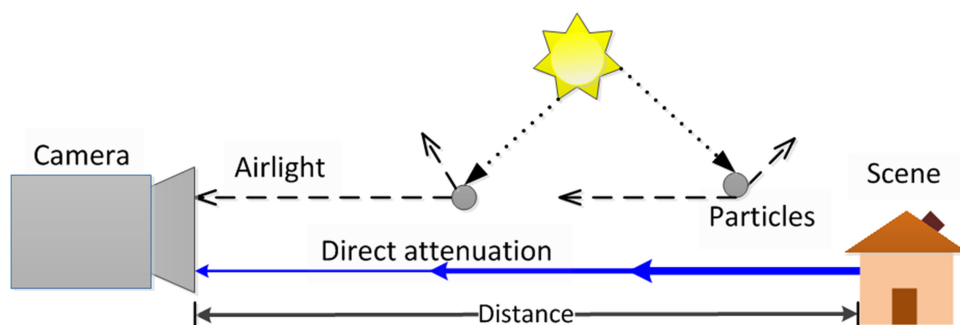
photonics
SOCIETY

IEEE

Fast Single-Image Dehazing Algorithm Based on Piecewise Transformation in Optical Model

Guoling Bi [ORCID],[1] **Lirong Wang,**[2] **Changzheng Chen,**[1]
Xingxiang Zhang,[1] **and Guoning Li**[1]

[1]Changchun Institute of Optics, Fine Mechanics and Physics, Chinese Academy of
Sciences, Changchun 130033, China
[2]School of Electronic and Information Engineering, Suzhou University, Suzhou 215000,
China

Abstract: Single-image dehazing techniques are extensively used in outdoor optical image
acquisition equipment. Most existing methods pay attention to use various priors to estimate
scene transmission. In this paper, a fast single-image dehazing algorithm is proposed
based on a piecewise transformation model between the minimum channels of the hazy
image and the haze-free image in optical model. The minimum channel of the haze-free
image is obtained by the piecewise transformation, which is a quadratic function model
that we establish for the dark region, and a linear transformation model is established
for the bright region. Using the minimum channels of the hazy image and the haze-free
image, a transmission estimation model is established based on the haze optical model with
adjustment variables. To obtain an accurate estimation of atmospheric light, we estimate the
atmospheric light twice. Finally, the haze-free image is restored. Experimental results show
that the proposed algorithm has minimal halo artifacts and color distortion in various depths
of field, flat areas and sky areas. From the subjective evaluation, objective evaluation and
running time analysis, it can be seen that the algorithm in this paper is superior to most
existing technologies.

Index Terms: Image dehazing, piecewise transformation, transmission map, minimum
channel.

1. Introduction

Images captured in hazy scenes often suffer from visibility reduction and color degradation due
to atmospheric scattering caused by atmospheric particles [1]–[3]. This not only affects human
visual perception but also has an adverse effect on video analysis applications, such as object
recognition, object tracking, and scene classification [4]–[6]. Therefore, performing dehazing on a
single image is critical and challenging for practical applications such as outdoor surveillance and
autonomous/assisted driving.

Image dehazing can be simply divided into conventional contrast enhancement methods and
physical model-based methods. The conventional contrast enhancement methods include his-
togram equalization and its variations [7]–[9], which are the most widespread nonphysical model

algorithms. Retinex-based methods [10]–[12] enhance image contrast in accordance with specific needs but without knowing the mechanism with image degradation. The advantage of these nonphysical model algorithms is that they are simple, but they easily introduce color distortion due to the lack of consideration for the degradation mechanisms of hazy images.

Improved results were obtained by employing physical-based models, which analyzed the image degradation mechanism of an image by building models to realize scene reconstruction. Researchers have proposed many dehazing algorithms using multiple images or depth information [13]–[17]. For example, polarization-based dehazing methods [13]–[15] use images taken with different degrees of polarization to obtain haze-free images effectively. Depth-based methods [16] require known 3D models or that the user inputs some depth information. In practice, multiple hazy images and/or depth information are not always available.

Hence, single-image haze removal algorithms have attracted extensive attention from researchers due to their simplicity and practicality. Most dehazing algorithms have payed attention to estimate transmission media [18]–[34]. For example, Fattal [18] assessed a transmission map by assuming that the albedos of the objects and the transmission were statistically uncorrelated. This method can not only restore impressive haze-free images but also provide a reliable transmission estimation for a hazy scene. However, this method may fail to recover a haze-free image when the required assumptions are broken. Tan *et al*. [19] maximized local radiance contrasts to remove haze by assuming that haze-free images have higher contrasts than hazy images. Nevertheless, the dehazing images with this method are often spotted by color distortion. He *et al*. [20] proposed the famous dark channel prior (DCP), which can achieve compelling haze-free images and has been widely used [21]–[26]. Later, the soft matting strategy in the DCP algorithm was replaced by a guided filter [27], which greatly improved processing efficiency. Tarel *et al*. [28] proposed a novel algorithm for visibility restoration based on a median filter to preserve both the edges and corners of an image, and this method was able to achieve better results than those of other methods in both color and gray-level images. However, the computational complexity rapidly increases as the size of the image rising. Meng *et al*. [29] obtained a transmission map using a boundary constraint assumption and contextual optimization. This scheme can effectively remove haze, but it exhibits color distortion for objects having a similar color to that of atmospheric light. Berman *et al*. [31] developed a nonlocal image dehazing algorithm based on the haze-lines prior; the algorithm can be performed well at the edges of images but lead to color cast in some cases. Bui *et al*. [33] proposed fast dehazing via the construction of color ellipsoids that were fitted statistically to hazy pixel clusters in RGB space; the transmission values were then calculated through color ellipsoid geometry. To overcome incorrect transmission estimation caused by a depth error in the skyline or wrong haze information, Shin *et al*. [34] presented a novel optimization-based dehazing algorithm that combined the radiance and reflectance components of an image with an additional refinement using a structure-guided l0-norm filter.

More recently, studies have focused on learning-based methods that can significantly improve the quality of image dehazing, and these methods have achieved promising performance in various visual tasks [35]–[36]. Several studies have used CNNs to predict transmission [37]–[39]. Zhang and Patel [40] proposed a densely-connected pyramid dehazing network (DCPDN), which used a joint discriminator to decide whether the dehazed result was real or fake. Generative adversarial networks (GANs) [41] have been used in image dehazing. Dong [42] proposed a multiscale boosted dehazing network (MSBDN) with dense feature fusion based on the U-Net architecture. Zhu *et al*. [30] proposed the color attenuation prior (CAP) and combined it with a data-driven approach. Wang *et al*. [43] proposed a straightforward but remarkable prior—the atmospheric illumination prior and applied multi-scale convolutional networks to identify hazy regions and restore deficient texture information automatically. Li *et al*. [44] proposed an encoder and decoder architecture which different from the generative network in basic conditional GANs, where the clear image is estimated by an end-to-end trainable neural network. However, these methods are limited in some applications where additional information or multiple images are not available, and single-image dehazing based on the haze-optical model has no such limitation.
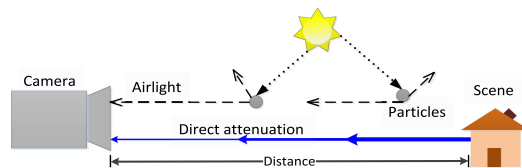
Fig. 1. The schematic of the optical model for a hazy scene.

In a word, the main difficulty in solving single-image dehazing is the pair of unknowns, atmospheric light and transmission, which makes it a severely ill-posed problems. Most existing methods solve this ill-posed problem based on priors or assumptions on transmission and scene radiance. However, some areas of a hazy image that do not conform to these priors or assumptions result in inaccurate transmission estimation, and haze-free bright pixels (such as white cars, lit headlights/street lights, sunlight, etc.) often cause imprecise atmospheric light estimation, which introduces halo artifacts and color distortion. Additionally, the computational speed is still a challenging issue that limits the application of these methods in real-time systems.

We propose a fast dehazing method based on a piecewise transformation that has less computational complexity than other methods. In this paper, the minimum channel of the haze-free image is divided into two parts, the dark region and the bright region, by the average of the minimum channel of the hazy image, establishing the piecewise transformation model between the minimum channels of the hazy image and the haze-free image, including the quadratic function model for the dark region and the linear transformation model for the bright region. Based on the haze optical model with adjustment variables, an optimized estimation model for pixel-level transmission is established by the minimum channels of the hazy image and haze-free image. The atmospheric light is estimated twice, the first is a preliminary estimate and the second is an accurate estimate. Finally recovering the haze-free image. The remainder of the paper is organized as follows. In Section II the haze optical model is introduced and analyzed. We present the proposed algorithms in Section III. In Section IV, subjective and objective experimental results and comparisons are demonstrated and discussed. Finally, conclusions are then drawn in Section V.

2. Related Works

2.1 Haze Optical Model

The haze optical model was proposed by McCartney [45] is widely used to describe the formation of a hazy image I(x), where x is the pixel index, and the model is usually depicted as

$$I(x) = J(x)t(x) + A(1 - t(x)) \tag{1}$$

Where J(x) is the scene radiance, A is the global atmospheric light, and t(x) is the medium transmission which indicates the portion of the light that is not scattered and reaches the camera. A schematic of the optical model for a hazy scene is shown in Fig. 1. The scattering of atmospheric particles is mainly divided into two parts: the first item is called direct attenuation which describes the scene radiance and its decay in the medium, as shown by the solid line in Fig. 1; the second item is called airlight which results from previously scattered light and leads to a shift in the scene color, as shown by the dotted line in Fig. 1. While the direct attenuation is a multiplicative distortion of the scene radiance, the airlight is an additive one. The main task of single image dehazing is to recover a haze-free image J(x), A, and t(x) from the received image I(x), and this is an under-constrained problem.

When the atmosphere is homogenous, the transmission t(x) can be expressed as [20]

$$t(x) = e^{-\beta d(x)} \tag{2}$$
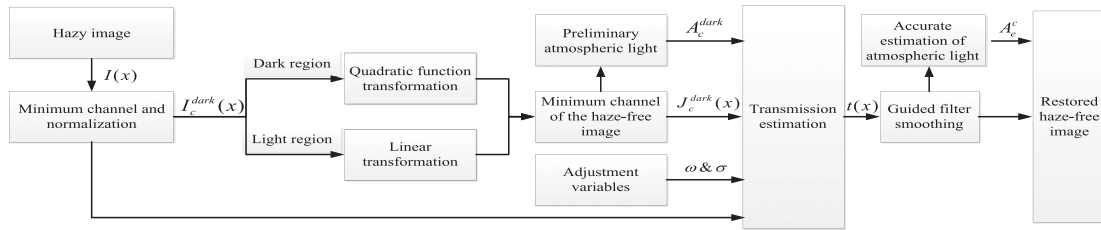
Fig. 2. Flow chart of the proposed method.

Where β is the global extinction coefficient of the atmosphere, and d(x) is the distance from the scene to the camera. This indicates that the scene radiance is attenuated exponentially with the scene depth and the global extinction coefficient. However, the exact values of the global extinction coefficient and the depth information of an image are difficult to obtain. If we have some prior knowledge about the single image that can be used to estimate the transmission and the atmospheric light, then J(x) can be resolved according to Eq. (1).

2.2 Transmission Estimation Based on Minimum Channels

From Eq. (1), the expression for transmission can be obtained as

$$t(x) = 1 - \frac{I(x) - J(x)}{A - J(x)} \tag{3}$$

Wang *et al*. [32] proposed that at least one reflection coefficient of the color component in a color image is very small, and given the transmission estimation with the minimum channels as

$$t(x) = 1 - \frac{I_c^{dark}(x) - J_c^{dark}(x)}{A_c^{dark} - J_c^{dark}(x)} \tag{4}$$

where $c \in \{r, g, b\}$, $I_c^{dark}(x) = \min_c (I^c(x))$ is the minimum channel of the hazy image, $J_c^{dark}(x) = \min_c (J^c(x))$ is the minimum channel of the haze-free image, $A_c^{dark} = \min_c (A^c)$ is the minimum of the atmospheric light of the radiation channel of the hazy scene, and t(x) is an estimate of the transmission. Here $I_c^{dark}(x)$ is a known quantity, A_c^{dark} is a constant, and only $J_c^{dark}(x)$ is an unknown quantity.

3. Proposed Algorithm

In this section, we present a fast single-image dehazing method based on the minimum channel piecewise transformation, the flow chart for this method is shown in Fig. 2. According to the atmospheric scattering model, the proposed method is divided into five parts: 1) The influence of $J_c^{dark}(x)$ on transmission estimation is analyzed which based on minimum channels. 2) A piecewise transformation model between $I_c^{dark}(x)$ and $J_c^{dark}(x)$ is proposed, then $J_c^{dark}(x)$ is obtained. 3) A single channel atmospheric light A_c^{dark} is estimated Using $J_c^{dark}(x)$, and adjustment variables (ω and σ) are introduced to optimize the transmission estimation model, and then the obtained transmission estimation is smoothed by guided filtering. 4) An accurate estimate of the three-channel atmospheric light A_e^c is obtained according to the smoothed t(x). 5) The haze-free image is restored based on the haze optical model.

3.1 The Influence of $J_c^{dark}(x)$ on Transmission Estimation

From Eq. (4), due to the existence of haze, the relationship between the minimum channels of the hazy image and the haze-free image is as follows: $I_c^{dark}(x) \geq J_c^{dark}(x)$, and t(x) $\leq$ 1. Assume that
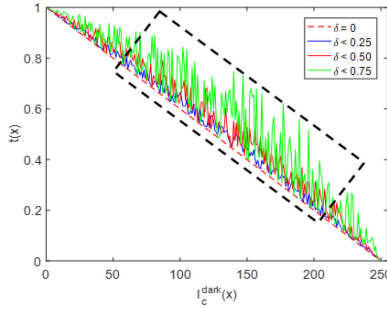
Fig. 3. The effect of different values of δ on transmission estimation.
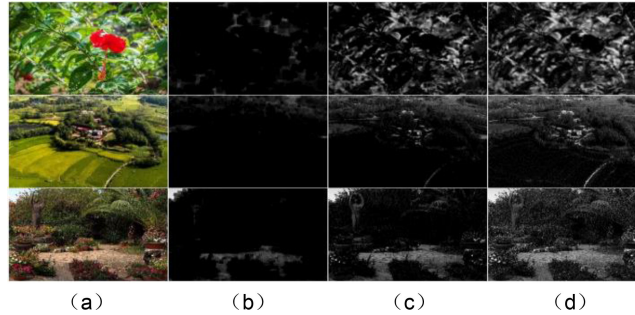
Fig. 4. The haze-free images and the minimum-filtered images with different radius. (a) The haze-free images. (b) r = 15. (c) r = 3. (d) r = 1.

there is a simple linear relationship between $I_c^{dark}(x)$ and $J_c^{dark}(x)$, such as $J_c^{dark}(x) = \delta I_c^{dark}(x)$, where $\delta \in [0, 1]$. We choose $\delta = 0$, $\delta < 0.25$, $\delta < 0.50$, and $\delta < 0.75$, obtain the random value of $\delta I_c^{dark}(x)$ (when $I_c^{dark}(x) \in [0, 255]$) to characterize the uncertainty of the value of $J_c^{dark}(x)$ and set $A_c^{dark} = 250$. The obtained t(x) is shown in Fig. 3.

It can be seen from Fig. 3 that when $\delta = 0$, that is $J_c^{dark}(x) \to 0$, $I_c^{dark}(x)$ and t(x) have a linear relationship, as indicated the red dashed straight line. When $\delta > 0$, that is, $J_c^{dark}(x) \not\to 0$, the value of t(x) increases as $I_c^{dark}(x)$ and $J_c^{dark}(x)$ increase. As δ increases, when the pixels value of $I_c^{dark}(x)$ are in the middle region (as shown by the black dotted rectangle in Fig. 3), the deviations from the red dashed straight line are larger than those of the two end regions. That is, when the pixel values of $I_c^{dark}(x)$ are in the middle region, the value of t(x) is most affected by $J_c^{dark}(x)$.

We select some sunny outdoor images from the Internet and carry out minimum filtering on them. The filter radius are r = 15, r = 3, and r = 1 (that is, the minimum channels). Here, we only provide three representative outdoor images and their minimum-filtered images, as shown in Fig. 4. According to the dark channel prior [20], due to the existence of a large number of outdoor shadows and bright colors, the dark pixels of the minimum-filtered image gradually increase as the filter radius increases. This is true even for r = 1, that is, the minimum-channel image also has a large number of dark pixels, namely, $J_c^{dark}(x) \to 0$. That is, when $\delta = 0$, the transmission estimate matches the red dashed straight line in Fig. 3. When the pixel values of $I_c^{dark}(x)$ are in the middle region, the transmission t(x) is overestimated according to Eq. (4). This requires our method to reduce the estimation of $J_c^{dark}(x)$ in the middle region, and this can increase the accuracy of the estimation of t(x). Therefore, we select the piecewise function to estimate $J_c^{dark}(x)$.
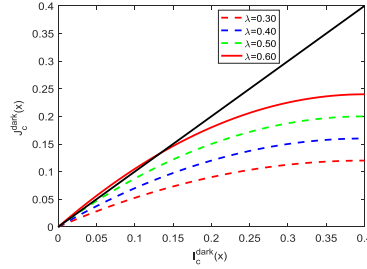
Fig. 5. Curves of the changes of $J_c^{dark}(x)$ with changes in $I_c^{dark}(x)$ under different values of λ.

3.2 The Piecewise Transformation Model

We normalize $I_c^{dark}(x)$ and $J_c^{dark}(x)$. Under hazy conditions, $J_c^{dark}(x)$ increases with the increase of $I_c^{dark}(x)$, so we assume that there is a positive correlation between them, which can be expressed by

$$J_c^{dark}(x) = \psi_c(I_c^{dark}(x)) \tag{5}$$

It can be seen that $\psi_c(x)$ is an increasing function, and the value range and definition range of $\psi_c(x)$ are both [0, 1]. The average of $I_c^{dark}(x)$ is M_I, and we choose this average as the threshold and divide $J_c^{dark}(x)$ into two regions. The region smaller than M_I is called the dark region, and the region larger than M_I is called the bright region.

In the dark region, the pixel values of images $J_c^{dark}(x)$ and $I_c^{dark}(x)$ are close, but as $I_c^{dark}(x)$ increases, $J_c^{dark}(x)$ gradually increases, and $J_c^{dark}(x) \leq I_c^{dark}(x)$, that is, the slope is less than or equal to 1. As analyzed in the previous section, we should reduce the estimation of $J_c^{dark}(x)$ in the middle region, that is, the rate of increase should gradually decrease with the increase of $I_c^{dark}(x)$ in the dark region. Therefore, we assume that $J_c^{dark}(x)$ and $I_c^{dark}(x)$ conform to the quadratic function relationship. The vertex of the quadratic function is set to $(M_I, \lambda M_I)$ and passes through the point $(0, 0)$, λ is a constant parameter, so it can be expressed as

$$J_c^{dark}(x) = -\frac{\lambda}{M_I}(I_c^{dark}(x) - M_I)^2 + \lambda M_I \tag{6}$$

The slope of the quadratic function is

$$k = -\frac{2\lambda}{M_I}(I_c^{dark}(x) - M_I) \tag{7}$$

When $I_c^{dark}(x) = 0$, the slope k takes the maximum value $k_{max} = 2\lambda$, and when $2\lambda \leq 1$, we can obtain $\lambda \leq 0.5$. We choose $M_I = 0.4$ when λ is 0.3, 0.4, 0.5 and 0.6 in the dark region, and when $I_c^{dark}(x) < M_I$, the corresponding relationship between $J_c^{dark}(x)$ and $I_c^{dark}(x)$ is shown in Fig. 5. The black straight line indicates that $J_c^{dark}(x) = I_c^{dark}(x)$. It can be seen that $J_c^{dark}(x) > I_c^{dark}(x)$ in the local area when $\lambda > 0.5$, which is unreasonable. Only when $\lambda \leq 0.5$ is the curve below the black straight line, which satisfies $J_c^{dark}(x) \leq I_c^{dark}(x)$.

In the bright region, that is, $I_c^{dark}(x) \geq M_I$, we assume that there is a linear relationship between $J_c^{dark}(x)$ and $I_c^{dark}(x)$, and the value range and definition range in Eq. (5) are both [0, 1]. Using boundary conditions, according to the calculation model for the dark region, it can be obtained that the linear function passes the points $(1, 1)$ and $(M_I, \lambda M_I)$, and the linear relationship is as follows:

$$J_c^{dark}(x) = \frac{1 - \lambda M_I}{1 - M_I} I_c^{dark}(x) + \frac{(\lambda - 1)M_I}{1 - M_I} \tag{8}$$
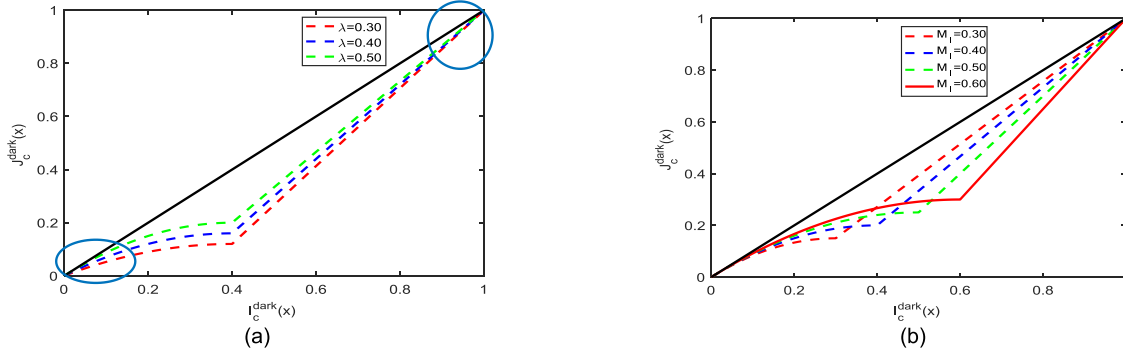
Fig. 6. The relationship between $I_c^{dark}(x)$ and $J_c^{dark}(x)$ for all dark and bright regions. (a) With different values of λ; (b) With different values of M_l.

Thus, we can obtain the piecewise functional relationship between $J_c^{dark}(x)$ and $I_c^{dark}(x)$ as

$$J_c^{dark}(x) = \begin{cases} -\frac{\lambda}{M_l}\left(I_c^{dark}(x)-M_l\right)^2 + \lambda M_l I_c^{dark}(x) < M_l \\ \frac{1-\lambda M_l}{1-M_l}I_c^{dark}(x) + \frac{(\lambda-1)M_l}{1-M_l} I_c^{dark}(x) \geq M_l \end{cases} \tag{9}$$

When λ is 0.3, 0.4 and 0.5, and $M_l = 0.4$, the relationship between $J_c^{dark}(x)$ and $I_c^{dark}(x)$ for all dark and bright regions is shown in Fig. 6(a). As λ decreases near to the value of $M_l = 0.4$, the curve is farthest away from the straight line of $J_c^{dark}(x) = I_c^{dark}(x)$.

In addition, using a lot of statistics, we have found that $\frac{M_J}{M_l} \leq 0.5$ in general, where M_J is the average of $J_c^{dark}(x)$. In this paper, we choose $\lambda = 0.5$, the average of $I_c^{dark}(x)$ is limited to $M_l \in [0.35, 0.65]$ in different hazy scenes, that is, when M_l is less than 0.35, we set $M_l = 0.35$; when M_l is greater than 0.65, we set $M_l = 0.65$. When the values of M_l are 0.3, 0.4, 0.5 and 0.6, the corresponding relationship between $I_c^{dark}(x)$ and $J_c^{dark}(x)$ is shown in Fig. 6(b).

Since haze causes the brightness of the image to become larger, the M_l corresponding to $I_c^{dark}(x)$ is also made larger. As M_l increases, near the value of M_l, the curve is farther away from the straight line of $J_c^{dark}(x) = I_c^{dark}(x)$, and the area enclosed by the piecewise function curve and the straight line of $J_c^{dark}(x) = I_c^{dark}(x)$ is increased, as shown in Fig. 6(b). The above analysis shows that when the value of $I_c^{dark}(x)$ is in the middle region (near the value of M_l), the relative distance of the deviation of $J_c^{dark}(x)$ from the straight line of $J_c^{dark}(x) = I_c^{dark}(x)$ is farthest, and it meets the requirements of the analysis in the previous section for reducing the estimated value of $J_c^{dark}(x)$ in the middle region.

3.3 Optimization of the Transmission Estimation Model

We substitute $J_c^{dark}(x)$ from Eq. (9) into Eq. (4) to obtain an estimate of the pixel-level transmission $t(x)$, where $\lambda = 0.5$.

$$t(x) = \begin{cases} 1 - \frac{I_c^{dark}(x)+\frac{1}{2M_l}(I_c^{dark}(x)-M_l)^2 - \frac{M_l}{2}}{A_c^{dark}+\frac{1}{2M_l}(I_c^{dark}(x)-M_l)^2 - \frac{M_l}{2}} I_c^{dark}(x) < M_l \\ 1 - \frac{I_c^{dark}(x)-\frac{2-M_l}{2-2M_l}I_c^{dark}(x)+\frac{M_l}{2-2M_l}}{A_c^{dark}-\frac{2-M_l}{2-2M_l}I_c^{dark}(x)+\frac{M_l}{2-2M_l}} I_c^{dark}(x) \geq M_l \end{cases} \tag{10}$$

The following process gives an estimate of the atmospheric light A_c^{dark}, and then it analyzes and optimizes $t(x)$.

3.3.1 Acquisition of the Atmospheric Light A_c^{dark}*:* According to Eq. (4), $A_c^{dark} = \min_c (A^c)$, and we consider that the area with the highest gray value for $J_c^{dark}(x)$ is the area for calculating the atmospheric light. Therefore, the top 0.1% of the pixels of in terms of the maximum values of $J_c^{dark}(x)$ are
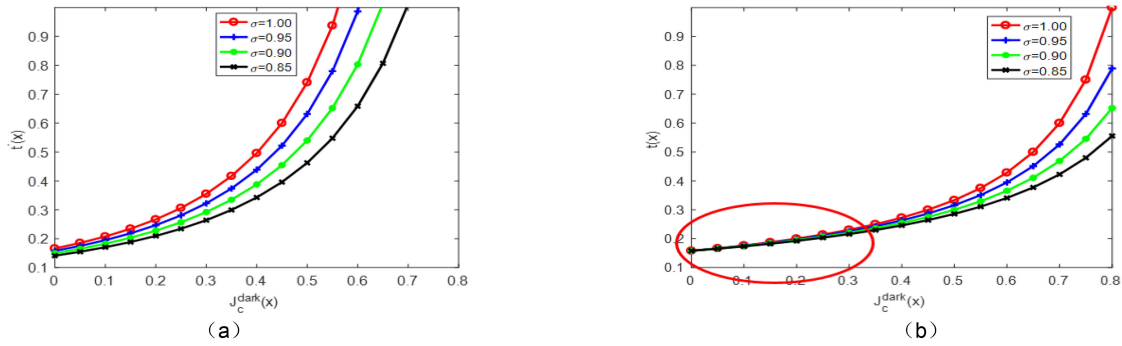
Fig. 7. Transmission derivatives and transmission estimates under different values of σ. (a) The derivatives of the transmission estimates. (b) The transmission estimates.

selected as the area for calculating the atmospheric light, where $\Omega_J \in 0.1\%\{top(count[J_c^{dark}(x)])\}$, the total number of pixels is N, and the average gray value of the three channels corresponding to the hazy image $I^c(x)$ is calculated as A^c, where $c \in \{r, g, b\}$. Then, the minimum value of the three channels A^c is obtained as the atmospheric light value $A_c^{dark} = \min\limits_c (A^c)$. The final expression is

$$A_c^{dark} = \min_{c \in \{r,g,b\}} \left(\frac{\sum_{x \in \Omega_J} I^c(x)}{N} \right) \tag{11}$$

3.3.2. Introduction of Adjustment Variables: To retain a very small amount of haze for the most distant objects, we choose to introduce an adjustment variable ω ($0 < \omega < 1$). When the value of $I_c^{dark}(x)$ is small (close to 0) or large (close to 1) (as shown by the blue ellipses in Fig. 6(a)), the value of $J_c^{dark}(x)$ is obtained according to Eq. (9) and is relatively close to $I_c^{dark}(x)$. As a result, in these local areas, the transmission t(x) calculated by Eq. (10) is relatively high. In general, due to the influence of haze, when $I_c^{dark}(x)$ is smaller (such as dark objects or shadows in close range), we think that the imaging distance is closer, and the t(x) obtained at this time is higher; this is in line with the actual situation. However, when $I_c^{dark}(x)$ is large (such as in the sky or in an area with dense haze in the distance), the imaging distance is far, the transmission estimated according to Eq. (10) is large, and the real transmission is small. To solve this problem, we introduce an adjustment variable σ in the transmission estimation model as

$$t(x) = 1 - \omega \frac{I_c^{dark}(x) - \sigma J_c^{dark}(x)}{A_c^{dark} - \sigma J_c^{dark}(x)} \tag{12}$$

We take the derivative of Eq. (12), and obtain the slope t'(x) as

$$t'(x) = \omega \frac{\sigma \left(A_c^{dark} - I_c^{dark}(x) \right)}{\left(A_c^{dark} - \sigma J_c^{dark}(x) \right)^2} \tag{13}$$

We choose $A_c^{dark} = 0.95$, $I_c^{dark}(x) = 0.8$ and $\omega = 1$; then, $J_c^{dark}(x) < 0.8$. When $\sigma = 1$, $\sigma = 0.95$, $\sigma = 0.9$ and $\sigma = 0.85$, the obtained t'(x) and t(x) are shown in Fig. 7. It can be seen that the smaller the value of σ, the smaller the value of t'(x) is, that is, the slower the t(x) growth rate is (as shown in Fig. 7(a)). When $J_c^{dark}(x)$ is held constant, the smaller σ is, the smaller the transmission t(x) (as shown in Fig. 7(b)). t(x) increases as $J_c^{dark}(x)$ increases; when $J_c^{dark}(x)$ increases and becomes close to $I_c^{dark}(x) = 0.8$, that is, $I_c^{dark}(x)$ is larger in the bright region than in the dark region (such as in the sky or in an area with dense haze in the distance), the transmission t(x) becomes smaller than the adjustment variable $\sigma = 1$, and this solves the problem of overestimating the transmission in the bright region.

In addition, the adjustment variable σ has little effect on the estimation of the transmission in the dark region (as marked by a red ellipse in Fig. 7(b)). This method achieves a good balance between

the dark and bright regions of the transmission estimation. In this paper, we choose $\sigma = 0.95$, which leads to an improvement in the dehazing result.

Since the proposed method depends on the grayscale information of the image, any change in the local transmission of the image should be relatively smooth. Therefore, we perform smooth processing and comprehensively compare the mean filter, Gaussian filter, bilateral filter and guided filter. Finally, the guided filter is selected for smoothing with high efficiency and good edge preservation.

3.4 Accurate Atmospheric Light Acquisition

In the previous section, we obtained a smooth and accurate transmission map. We assume that the area with the smallest transmission is the area with the highest haze density. We select the top 0.05% of pixels in terms of the minimum values of the transmission map as the area $\Omega_t \in$ 0.05%{down(count[t(x)])} to calculate atmospheric light. The total number of pixels is M, and the average gray value of the three channels of the hazy image $I^c(x)$ is calculated, thereby obtaining the accurate atmospheric light A_e^c of the three channels as

$$A_e^c = \left(\frac{\sum_{x \in \Omega_t} I^c(x)}{M} \right)_{c \in \{r,g,b\}} \tag{14}$$

3.5 Recovering the Scene Radiance

After the above modeling and analysis are completed, the transmission t(x) and atmospheric light A_e^c are obtained. According to the haze optical model in Eq. (1), the final haze-free scene is recovered as

$$J(x) = \frac{I(x) - A_e^c}{\max(t(x), t_0)} + A_e^c \tag{15}$$

t_0 is an adjustment variable, and we set it to 0.01. The image recovered by Eq. (15) looks dim, and we use the automatic color gradation method to enhance it.

4. Experimental Results

4.1 Display of the Related Results

Since the proposed algorithm is greatly influenced by the gray value of the hazy image, we choose two hazy images named 'Cones' and 'Sweden' for testing. The 'Cones' image is a hazy image with monotonous color, small areas of sky and no interference from white objects (as shown in the first line of Fig. 8). 'Sweden' is a hazy image with rich color, sky areas and white car interference (as shown in the second line of Fig. 8).

4.1.1. The Minimum Channel and Atmospheric Light Estimation: The averages of the 'Cones' image and 'Sweden' image are $M_I = 0.3759$ and $M_I = 0.6100$, respectively. The minimum-channel image $I_c^{dark}(x)$ is obtained as shown in Fig. 8(a). According to Eq. (9), $J_c^{dark}(x)$ is shown in Fig. 8(b). According to Eq. (11) and Eq. (14), the two estimated atmospheric lights of the 'Cones' image are $A_c^{dark} = 0.7431$ and $A_e^c = [0.7456, 0.7623, 0.7664]$; the two estimated atmospheric lights of the 'Sweden' image are $A_c^{dark} = 0.9883$ and $A_e^c = [0.9915, 0.9955, 0.9967]$. The positions are used to calculate the atmospheric light which marked with red pixels in the hazy image, as shown in Fig. 8(c) and Fig. 8(d).

The white car in the 'Sweden' image interferes with the proposed algorithm. For the initial estimation of the atmospheric light A_c^{dark}, 2.54% of the pixels are taken from the white car (the area marked by the black circle in Fig. 8(c)). For the final estimation of the atmospheric light A_e^c, the positions of the pixels are all in the distant sky area (as shown in the area marked by the black rectangle in Fig. 8(d)). The proposed algorithm enhances the robustness of the correct estimation of atmospheric light
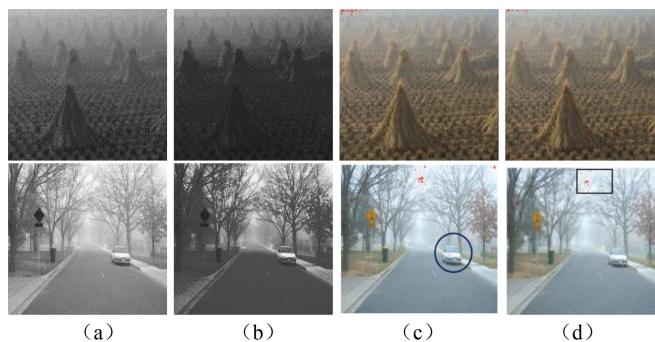
Fig. 8. Dark channel and atmospheric light estimation in hazy and haze-free scenes. (a) Minimum channel image $I_c^{dark}(x)$. (b) Minimum channel image $J_c^{dark}(x)$. (c) Preliminary estimation of atmospheric light. (d) Accurate estimation of atmospheric light.
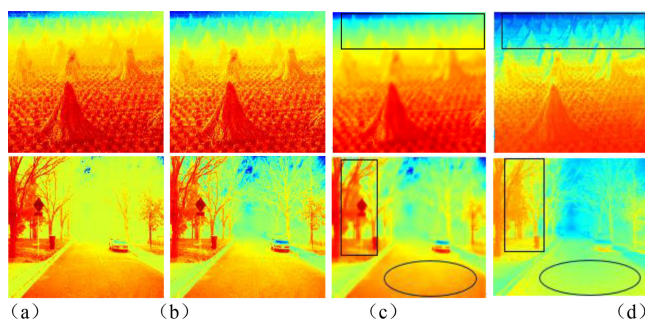
Fig. 9. Transmission estimation. (a) σ not introduced. (b) σ introduced. (c) Guided filtering. (d) He's method [20].

4.1.2. Transmission Estimation: To demonstrate the effect of transmission estimation clearly, we use a pseudocolor image to display the transmission map, as shown in Fig. 9 (redder parts indicate high values and bluer parts indicate low values). For the transmission estimation model, as shown in Eq. (10), the estimated result is shown in Fig. 9(a). In the sky area and the low transmission area with a large depth of field, the transmission is overestimated. When σ is introduced, the transmission estimation model is used, as shown in Eq. (12), and the result of transmission estimation is shown in Fig. 9(b). It can be seen that the estimation of the lower transmission areas are more accurate after introducing variable σ (as shown in the blue area in Fig. 9(b)). After guided filtering, the transmission images are smoothed and the edges are maintained, as shown in Fig. 9(c).

Compared with the estimated transmission map of the dark channel by He [20] (see Fig. 9(d)), the estimates of the transmission map in the distant view (as shown in the first row of black rectangles in Fig. 9(c) and 9(d)), close-up trees and traffic signs (as shown in the second row of black rectangles in Fig. 9(c) and 9(d)), and the pavement in the close-range view (as shown in the second row of black ellipses in Fig. 9(c) and 9(d)) by the proposed method are all estimated more accurately. The estimated transmission of the dark channel by He [20] is obviously low, and this causes the image to be very dark or contain color distortion after dehazing (as shown by the subjective evaluation of the dehazing results in the next section). The results show that our transmission map contains more detail and truly reflects the underlying scene content, and our transmission map is more accurate than the one by He *et al*. [20].
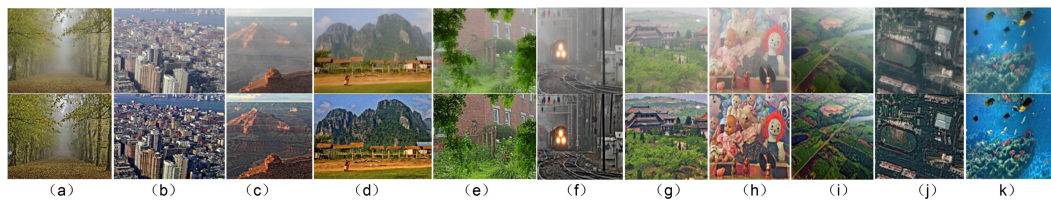
Fig. 10. Some of the experimental results of the proposed method.
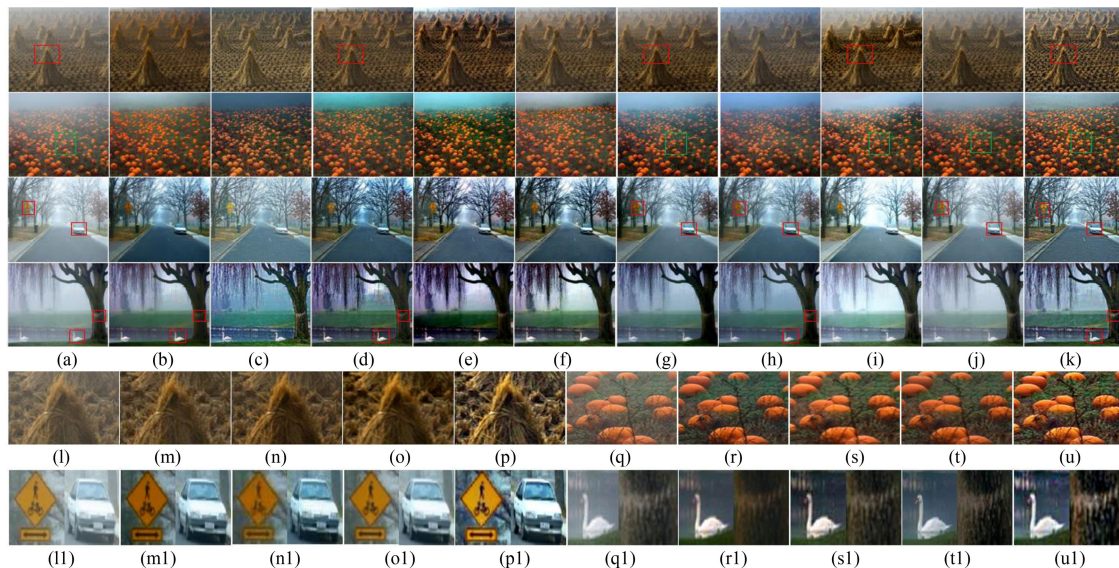
Fig. 11. Comparison of the results of different methods on single hazy images. (a) Input hazy image. (b) He's method [20]. (c) Tarel's method [28]. (d) Meng's method [29]. (e) Berman's method [31]. (f) Shin's method [34]. (g) DehazeNet [38]. (h) CAP [30]. (i) DCPDN [40]. (j) MSBDN [42]. (k) Our method. (l)–(o) are the enlarged images marked with rectangles in (a), (d), (g), (i) and (k). (q)–(u) are the enlarged images marked with rectangles in (a), (g), (i), (j) and (k). (l1)–(p1) are the enlarged images marked with rectangles in (a), (g), (h), (j) and (k). (q1)–(u1) are the enlarged images marked with rectangles in (a), (b), (d), (h) and (k).

4.2 Subjective Evaluation

Some of the experimental results are shown in Fig. 10, including a total of eleven groups of experimental images. For each group, the upper row shows the original hazy images, and the lower row shows the dehazed images. Whether the depths of field of the images are large or small, whether the colors of the images are rich or monotonous, and whether the details of images are rich or insufficient, the proposed method can obtain images with natural colors and clear details under all different conditions. The dehazing method can process images of different application scenarios effectively, including common outdoor images, aerial images (Fig. 10(i)), satellite remote sensing images (Fig. 10(j)), and underwater images (Fig. 10(k)). Therefore, the algorithm in this paper has the potential to deal with hazy images in a wide range of applications.

4.2.1. Hazy Images with Different Color Complexities: Considering differences in color complexity, we choose two groups of hazy images, where the colors of the images 'Cones' and 'Pumpkins' in the first and second row of Fig. 11 are monotonous. The colors of the images 'Sweden' and 'Geese' in the third and fourth rows of Fig. 11 are rich and contain white regions that are hard to handle because most existing dehazing methods are sensitive to the white color. We compare our results with those of nine state-of-the-art visibility restoration algorithms: He's [20], Tarel's [28],
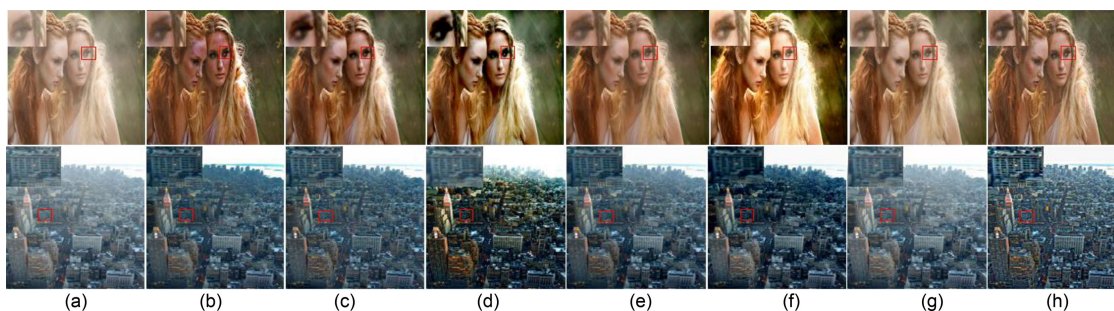
Fig. 12. Comparison of the results of different methods on single hazy images. (a) Input hazy images. (b) He's method [20]. (c) Shin's method [34]. (d) Berman's method [31]. (e) DehazeNet [38]. (f) DCPDN [40]. (g) MSBDN [42]. (h) Ours method.

Meng's [29], Berman's [31], Shin's [34], DehazeNet [38], CAP [30], DCPDN [40], and MSBDN [42]. In this paper, all the dehazing methods that are chosen for comparison purposes have code or different recovery images that can be easily downloaded from the author's website.

Fig. 11(a)–Fig. 11(j) are the hazy images and dehazing results. In Fig. 11(b), He's [20] method underestimates the transmission of trees, traffic signs and streets in the close range which causes the dehazed image to become very dark or even distorted in these areas. Similarly, Berman's [31], Meng's [29] and Shin's [34] algorithms also cause the image to become very dark due to the low transmission estimates, such as the trees in hazy images with rich color (Fig. 11(d) - Fig. 11(f)). However, in hazy images with monotonous colors, these three methods often suffer from insufficient dehazing and color distortion.

Although the dehazing results of Tarel's [28] (Fig. 11(c)) are not change to dark in both either the near or distant scenes, the haze removal ability of the algorithm is insufficient which leads to bad visual results. In comparison, the learning-based methods have high color fidelity, but the CAP [30] (Fig. 11(h)) and MSBDN [42] (Fig. 11(j)) methods tend to leave haze in the results. The DehazeNet [38] (Fig. 11(g)) and DCPDN [40] (Fig. 11(i)) methods are effective in removing haze in close regions but looks blurry in distant regions because the learned features usually cause overestimated transmission maps. It can be seen that whether the color is monotonous or rich, our results (Fig. 11(k)) have high contrast and realistic color because our method can accurately estimate transmission and atmospheric light.

We select representative areas (marked by rectangles) from the dehazing results of different methods to zoom in, as shown in the fifth and sixth rows of Fig. 11. The enlarged images show that although the proposed method depends on the gray values of the images, it is not been affected by white objects (such as white cars and white geese). These bright objects are recovered very well, and other scenes of the images are recovered with rich details and high color fidelity. It is better than the other algorithms in the dehazing stability.

4.2.2. Hazy Images with Different Depths of Field: The classical hazy images 'Girls' and 'NewYork2' have shallow and large depths of field respectively (as shown in Fig. 12 (a)). We choose them as the second group images for qualitative comparison. Fig. 12 (b) - Fig. 12 (f) show the results of He's method [20], Shin's method [34], Berman's method [31], DCPDN [40], MSBDN [42] and the proposed method, respectively.

In the first row of Fig. 12, He's [20], Berman's [31] and DCPDN [40] algorithms improve the contrast significantly, but the colors of the images are obviously distorted. Shin's method [34], DehazeNet [38], MSBDN [42] and our method achieve better dehazing results than the other three methods, and the partial images outlined by the red rectangles in the dehazing results are enlarged, as shown in the upper left corner of Fig. 12. It can be seen that our algorithm can overcome the color distortion and yield good visual results with many details and high contrast.
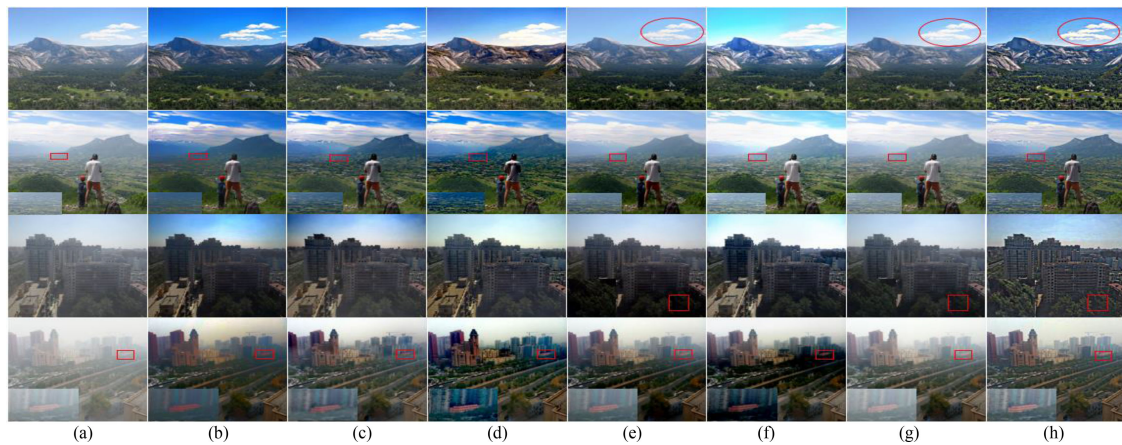
Fig. 13. Comparison of the results of different methods on single hazy images. (a) Input hazy images. (b) He's method [20]. (c) Shin's method [34]. (d) Berman's method [31]. (e) DehazeNet [38]. (f) DCPDN [40]. (g) MSBDN [42]. (h) Our method.

In the second row of Fig. 12, Berman's method [31] and DCPDN [40] also obviously suffer from color distortion, especially for long-shot scenery. Although the dehazing results of MSBDN [42] not darkened or brightened, the haze removal ability is insufficient and the dehazed image is still very blurry. Compare with He's method [20], DehazeNet [38] and Shin's method [34], the proposed method avoids color distortion and have clear structures. The enlarged images are outlined by the red rectangles as shown in the upper left corner of Fig. 12.

4.2.3. Hazy Images with Sky Areas: The sky region with a hazy image is a challenge for dehazing methods, because clouds and haze are similar natural phenomena with the same atmospheric scattering model [40]. Two widely-used test images with large sky areas ('Mountain' and 'Man') are commonly chosen in dehazing papers, as shown in the first and second rows of Fig. 13, respectively. We also choose two real-world outdoor hazy images from the test subset SOTS of the RESIDE dataset [46] for testing as shown in the third and fourth rows of Fig. 13. All the results are compared with those of six state-of-the-art methods: He's [20], Shin's [34], Berman's [31], DehazeNet [38], DCPDN [40], and MSBDN [42].

As shown in Fig. 13, the details of the scenes and objects are effectively restored by He's method [20], Shin's method [34], Berman's method [31] and DCPDN [40]. However, the results significantly suffer from color distortion and halo artifacts in the sky regions. Overall, the sky regions of these images are much darker than they should be which are oversaturated and distorted. DehazeNet [38], MSBDN [42] and our method have the most competitive visual results. In sky regions, such as the areas marked by red ellipses in the first row of Fig. 13, all three methods seem to be able to maintain the natural colors of the sky regions, but our method has more cloud edge details than the other two methods.

In the near shots, such as the enlarged images of the areas marked by rectangles in the third row of Fig. 13, the DehazeNet [38] method restore the trees to black (as shown in Fig. 13(e)), losing the original information of the trees, while the lighter colors of the images output by MSBDN [42] enable us to distinguish the details. However, the dehazed images with natural colors and easily distinguished details are obtained by the proposed method.

At medium distances, as shown in the enlarged images of the areas marked by rectangles in the second row of Fig. 13, it can be seen that the dehazing ability of MSBDN [42] is insufficient and that the contrasts of the dehazed images are low, while the dehazed images of DehazeNet [38] and the proposed algorithm have high contrast and clear details.

From the enlarged region of the images marked by rectangles in the lower left corner in the fourth row of Fig. 13, compared with Berman's method [31], DehazeNet [38] and MSBDN [42], we can
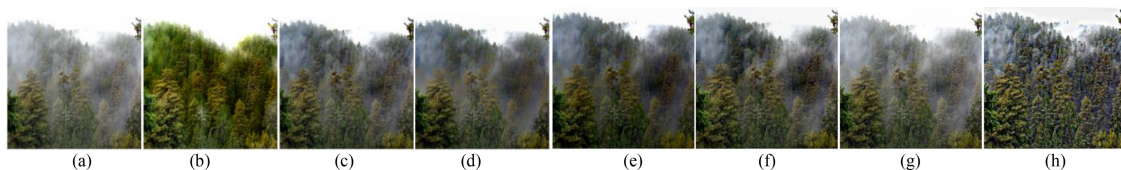
Fig. 14. Comparison of the results of different methods on single hazy images. (a) Input hazy images. (b) Fattal's method [18]. (c) Shin's method [34]. (d) CAP [30]. (e) DehazeNet [38]. (f) DCPDN [40]. (g) MSBDN [42]. (h) Our method.

find that the proposed method can obtain higher contrast while retaining the fine structures and natural colors, even for some regions that are far away from the camera.

From the above analysis of Figs. 13, the proposed method can achieve a promising dehazing effect with little color distortion and few halo artifacts in the sky. The details are enhanced, and the contrast is improved in each imaging ranges. It shows outstanding performance compared to some of the well-known methods in terms of human visual perception thanks to the effectiveness of the transmission estimation model and the doubly-accurate estimation of atmospheric light.

4.2.4. Hazy Images with Inhomogeneous Haze: The above experiments all deal with homogeneous haze in outdoor images. In fact, the proposed algorithm can also be applied to remove inhomogeneous haze and dense haze. Here, we select an image with inhomogeneous haze (Fig. 14(a)) from Fattal's paper and compare with the images output by Fattal's method [18], Shin's method [34], CAP [30], DehazeNet [38], DCPDN [40], MSBDN [42] and our method.

The results of Shin's algorithm [34], CAP [30] and DehazeNet [38] look very dim, and the details are not clear (Fig. 14(b)). DCPDN [40] and MSBDN [42] tend to leave haze in the results. Even if Fattal's algorithm can remove the haze more completely than our method, the sky region is too bright, and the colors of some tree regions are too light (Fig. 14(b)). Our algorithm employs a piecewise model transformation, which obtains estimation of the transmission map accurately and keeps a very small amount of haze subtly, resulting in a natural recovery of the image, as shown in Fig. 14(h).

4.3. Objective Evaluation

In this section, we choose reference and non-reference image quality assessment metrics to evaluate the performance of the compared methods in terms haze removal. Four images named 'Cones', 'Pumpkins', 'Sweden' and 'Geese' in Fig.12 are selected to test the results of He's method [20], Tarel's method [28], Meng's method [29], CAP [30], Berman's method [31], Shin's method [34], DehazeNet [38], DCPDN [40], MSBDN [42] and ours.

Firstly, the rate of new visible edges 'e' and mean ratio 'r' of the gradients at visible edges [47]–[48] are chosen as the reference image quality assessment metrics. High values of 'e' and 'r' obtained by a method indicate that the method achieves a better performance than others. We calculate 'e' and 'r' for an objective comparison of the haze removal effects achieved by different methods, as shown in Fig. 15 and Fig. 16, respectively. Fig. 15 shows that the value of 'e' obtained by our algorithm is close to or higher than those of the other compared algorithms. In Fig. 16, we can see that the value 'r' obtained from the images by our method are the highest among these dehazing methods.

Secondly, we use the popularity of the full reference PSNR and SSIM metrics to evaluate the dehazing results, and select two images in the SOTS dataset (the third and fourth rows of Fig. 13) for experiments, as shown in Table 1. It can be seen that although MSBDN [42] method is insufficient to remove the haze, it has obtained the highest PSNR and SSIM. This is not only due to the small distortion of the MSBDN [42] method, but also the ground truth of outdoor images in the SOTS dataset are related to a certain amount of haze. Although Berman's [31] method obtain
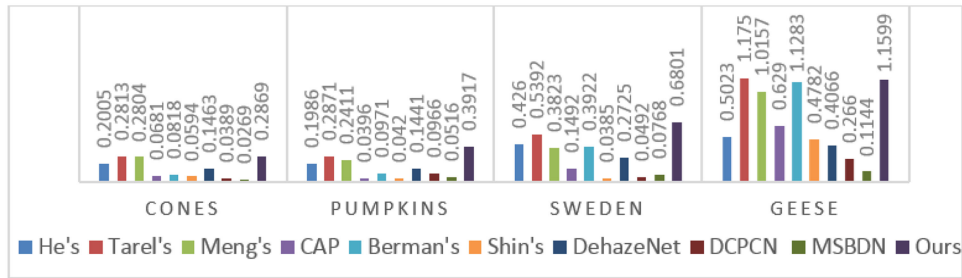
Fig. 15. Experimental data histograms of 'e' .
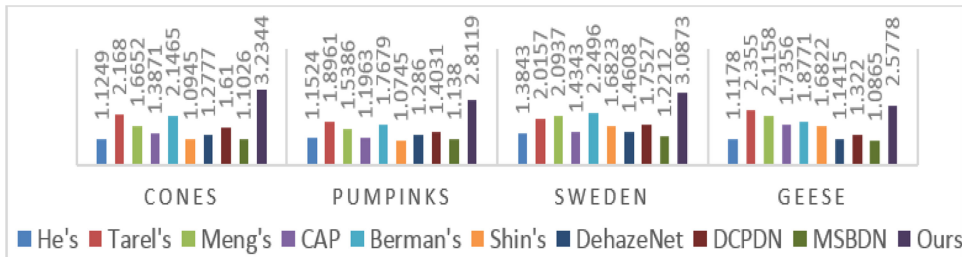
Fig. 16. Experimental data histograms of 'r'.

TABLE 1

Objective Comparison of SSIM and PSNR

Index		He's	Shin's	Berman 's	DehazeNet	DCPDN	MSBDN	Ours
3rd row of Fig. 13	SSIM	0.8656	0.8983	0.9161	0.8698	0.9804	**0.9825**	0.9039
	PSNR	16.5860	17.3845	21.9029	20.5780	20.1812	**25.2497**	24.8413
4th row of Fig. 13	SSIM	0.8001	0.8493	0.6798	0.7690	0.7002	**0.9720**	0.9150
	PSNR	12.9665	14.9043	11.7842	14.0299	12.1046	**23.9210**	23.0069

the PSNR and SSIM in third row of Fig. 13 are similar to ours, the values obtained in fourth row of Fig. 13 are too small. Among the remaining results, our method obtains higher PSNR and SSIM.

Thirdly, the mean square error (MSE) and image information entropy (IIE) were chosen as non-reference image quality assessments to evaluate the image dehazing performance [23]. If the MSE and the IIE are larger, it indicates a better performance by the image dehazing method being examined, that is, the method makes the image details clear and the contrast high. We calculate the MSE and the IIE for an objective comparison of different dehazing methods, as shown in Table 2. The MSEs of the images dehazing by the method of Berman's [31] and DCPDN [40] are higher than those of our algorithm, because the Berman's [31] method produce serious overcorrections in the images, making the image contrasts higher and the MSE larger. The dehazed images are obtained by DCPDN [40] method with very clear details in the near shot, resulting in high MSE values, but poor dehazing ability in the distance.

Finally, we have found that BeDDE is a real-world benchmark dataset for evaluations of dehazing methods. Six images of Beijing with medim or heavy fog concentration were selected of this dataset for the experiments, they are beijing_2.png, beijing_4.png, beijing_5.png, beijing_6.png, beijing_11.png and beijing_13.png. The clear images and mask images of Beijing are shown in Fig. 17. We compared them with VI [49], RI [49], VSI [50], GMSD [51] and FMI [52] as shown in Table 3. The VI, RI and VSI of the dehazed images are highest by our method, although the values of GMSD and FMI are not the highest, they are also very close to the highest value of He_Gd's method and CAP method, which fully demonstrate the effectiveness of our method.

TABLE 2
Objective Comparison of IIE and MSE

Methods	Cones		pumpkins		Sweden		Geese	
	IIE	MSE	IIE	MSE	IIE	MSE	IIE	MSE
Original	7.1037	35.5133	7.3851	45.9309	7.2304	40.0875	7.4718	53.2597
He's	7.0551	36.0522	7.3044	42.2655	7.4593	54.7224	7.5466	55.0252
Tarel's	6.9353	32.2973	6.9352	32.2967	7.1726	41.1644	7.6079	50.1155
Meng's	7.1331	38.0811	7.1325	38.0802	7.3912	51.6771	7.3448	48.1442
CAP	7.2517	39.9612	7.3058	41.2538	7.4408	51.2567	7.4429	46.5026
Berman's	7.5262	**57.3134**	7.5255	**57.3132**	7.5151	**59.1447**	7.3900	**67.6968**
Shin's	6.9402	33.8264	7.1374	40.1593	7.6118	57.5774	7.8188	57.9453
DehazeNet	7.2294	38.9216	7.5099	51.7188	7.5565	53.3533	7.5259	57.7979
DCPDN	7.4177	**51.7433**	7.471	**57.3127**	7.5135	**63.0138**	7.7615	**68.1848**
MSBDN	7.1273	36.8818	7.2831	43.9700	7.5075	49.7006	7.5716	56.0567
Ours	**7.5295**	**50.8813**	**7.6036**	**55.7849**	**7.6175**	**58.1873**	**7.9926**	**65.2983**

(a) Clear image   (b) Mask image

Fig. 17. The clear image and mask image of Beijing.

TABLE 3
Other Objective Comparisons

Method	VI	RI	VSI	GMSD	FMI
He_Gd's	0.88933	0.98984	0.94849	0.13513	**0.89728**
CAP	0.79454	0.97718	0.89506	**0.15406**	0.82117
DehazeNet	0.86726	0.99202	0.94988	0.14488	0.88480
DCPDN	0.87314	0.99201	0.95067	0.14146	0.89323
Ours	**0.89043**	**0.99241**	**0.9556**	0.14612	0.89348

4.4. Running Time Analysis

To verify the speed advantage of the proposed method, various images in this paper with different resolutions are tested. To ensure the fairness of the comparison, we select the methods whose open source code are running in the MATLAB environment, which are He's method [20], Tarel's method [28], Meng's method [29], CAP[30], Berman's method [31], Shin's method [34], DehazeNet [38]. Here, He_Gd is the DCP+guided filtering method [27].

All of the algorithms are implemented in MATLAB 64-bit on a DELL notebook computer equipped with an Intel Core i7-4712HQ processor @2.3 GHz and 16 GB memory. According to the size of the image resolution (increasing from small to large), Table 3 lists the running-times of the eight dehazing methods from top to bottom. In order to present the data in Table 4 more intuitively, we present it in the form of a graph as shown in Fig. 18.

From Table 4, we can see that when the image resolution is lower than 576×768, Berman's [31] algorithm is the most time-consuming. As the resolution increases, Tarel's [28] method takes the longest time. When the image resolution is 576×768, Tarel's method takes up to 22.746 s. Because Tarel's [28] method is optimized using a median filter, its computational complexity increases rapidly and it has the maximum slope (as shown by the red curve in Fig. 18). In Fig. 18, as the image size

TABLE 4
Running Times of Different Methods (Unit: S)

Resolution	He_Gd's	Tarel's	Meng's	CAP	Berman's	Shin's	DehazeNet	Ours
452×376	1.632	2.994	2.981	0.878	8.134	2.758	1.4359	**0.695**
511×381	1.865	3.427	3.621	0.953	8.452	3.383	1.509	**0.827**
600×400	2.972	5.133	4.233	1.117	9.149	3.415	1.876	**1.062**
576×768	4.121	**22.746**	6.549	2.917	11.093	6.224	3.841	**2.177**
1024×768	7.975	57.224	10.483	4.123	13.776	10.653	6.273	**3.831**
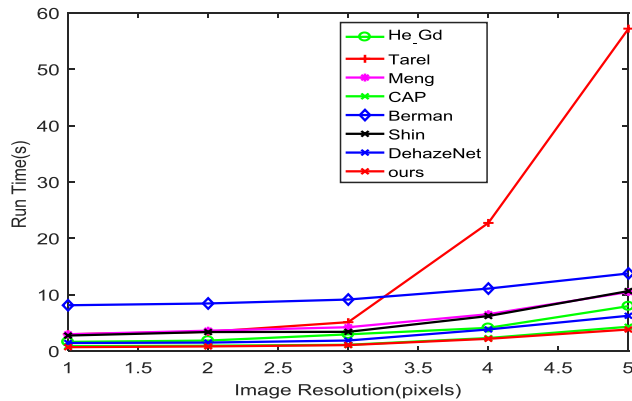
Fig. 18. Curves of relative time changing with the image size.

（a）   （b）   （c）
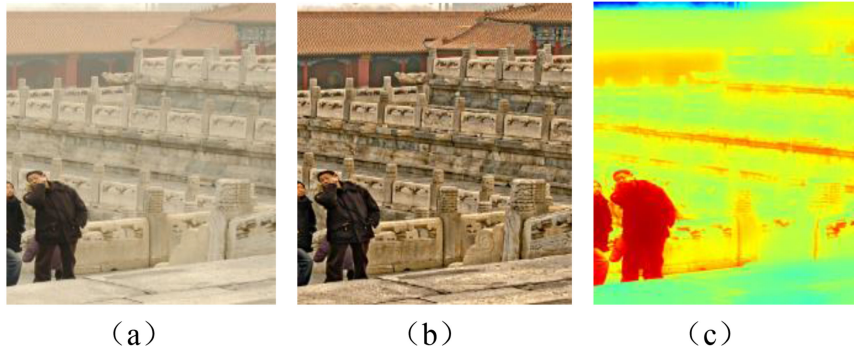
Fig. 19. Failure of the proposed method. (a) Input image. (b) Our result. (c) Our transmission map.

increases, the time consumed by He's method [20], Meng's method [29], CAP [30], Shin's method [30], DehazeNet [38] and ours gradually increase. The running time of CAP [30] is comparable to our method, but as the resolution increases, the running time of CAP [30] method is slightly higher than ours, because the time-consumption curve for our method has the smallest slope.

5. Conclusion

For a single hazy image, a fast dehazing method based on a piecewise transformation model is proposd. Taking the average of the minimum channels of the hazy image as the threshold, the minimum channels of the haze-free image are divided into two regions: a dark region and a bright region. Establishing the piecewise transformation model for the minimum channels of the hazy image and haze-free image, including the quadratic function model for the dark region and the linear transformation model for the bright region, enables us to obtain the minimum channel of the haze-free image. Based on the haze optical model, the estimation of the transmission model is

established by the minimum channels of the hazy image and the haze-free image. In view of the problem of overestimation of transmission in areas with large depths of field, an adjustment variable is introduced to optimize the transmission estimation model.

The atmospheric light is estimated twice, the initial estimation is used to obtain a single channel of atmospheric light based on the minimum channel of the hazy image, thereby obtaining a pixel-level transmission estimate, and guided filtering is used for local smoothing and edge detail retention. The smoothed transmission map is used to adaptively obtain a highly accurate global atmospheric light. Finally, the haze-free image is recovered.

To perform comparisons of our method with the other state-of-the-art methods qualitatively and quantitatively, a series of experiments are additionally implemented to demonstrate that the proposed algorithm obtains high-quality, haze-free images with abundant distinguishable details, low color distortion and few halo artifacts. The proposed method can not only meet the visual requirements of applications in subjective terms but it also has great advantages in terms of implementation efficiency.

However, the proposed algorithm is not suitable for some specific images. When an object in a large-area scene is essentially similar to atmospheric light, no shadow is projected on them (as shown for white marble in Fig. 19(a)). The minimum channel of scene radiation has bright values near such objects. As a result, our method could underestimates the transmission of these objects (as shown in Fig. 19(c)), which causes images to darken and contains color deviations after dehazing, as shown in Fig. 19 (b). For future work, we will conduct research on such images to improve the robustness of the algorithm to meet the needs of various practical application scenarios.

Acknowledgment

References

[1] J. P. Oakley and B. L. Satherley, "Improving image quality in poor visibility conditions using a physical model for contrast degradation," *IEEE Trans. Image Process.*, vol. 7, no. 2, pp. 167–179, Feb. 1998.

[2] S. K. Nayar, and S. G. Narasimhan, "Vision in bad weather," in *Proc. IEEE Conf. Comput. Vis.*, vol. 2, Sep. 1999, pp. 820–827.

[3] S. G. Narasimhan and S. K. Nayar, "Vision and the atmosphere," *Int. J. Comput. Vis.*, vol. 48, no. 3, pp. 233–254, Jul. 2002.

[4] Z. Tu, X. Chen, A. L. Yuille, and S.-C. Zhu, "Image parsing: Unifying segmentation, detection, and recognition," *Int. J. Comput. Vis.*, vol. 63, no. 2, pp. 113–140, 2005.

[5] B. Li *et al.*, "Benchmarking single-image dehazing and beyond," *IEEE Trans. Image Process.*, vol. 28, no. 1, pp. 492–505, Jan. 2019.

[6] J.-P. Tarel, N. Hautière, A. Cord, D. Gruyer, and H. Halmaoui, "Improved visibility of road scene images under heterogeneous fog," in *Proc. IEEE Intell. Veh. Symp.*, Jun. 2010, pp. 478–485.

[7] J. A. Stark, "Adaptive image contrast enhancement using generalizations of histogram equalization," *IEEE Trans. Image Process.*, vol. 9, no. 5, pp. 889–896, May 2000.

[8] T. K. Kim, J. K. Paik, and B. S. Kang, "Contrast enhancement system using spatially adaptive histogram equalization with temporal filtering," *IEEE Trans. Consum. Electron.*, vol. 44, no. 1, pp. 82–87, Feb. 1998.

[9] J. Y. Kim, L. S. Kim, and S. H. Hwang, "An advanced contrast enhancement using partially overlapped sub-block histogram equalization," *IEEE Trans. Circuits Syst. Video Technol.*, vol. 11, no. 4, pp. 475–484, Apr. 2001.

[10] D. J. Jobson, Z. Rahman, and G. A. Woodell, "A multiscale retinex for bridging the gap between color images and the human observation of scenes," *IEEE Trans. Image Process.*, vol. 6, no. 7, pp. 965–976, Jul. 1997.

[11] Z. Rahman, D. J. Jobson, and G. A. Woodell, "Retinex processing for automatic image enhancement," *J. Electron. Imag.*, vol. 13, no. 1, pp. 100–111, Jan. 2004.

[12] J. Li, "Application of image enhancement method for digital images based on retinex theory," *Optik - Int. J. Light Electron Opt.*, vol. 12, no. 4, pp. 5986–5988, 2013.

[13] Y. Y. Schechner, S. G. Narasimhan, and S. K. Nayar, "Polarization-based vision through haze," *J. Appl. Opt.*, vol. 42, no. 3, pp. 511–525, 2003.

[14] L. Shen *et al.*, "An iterative image dehazing method with polarization," *IEEE Trans. Multimedia*, vol. 21, no. 5, pp. 1093–1107, 2019.

[15] F. Liu *et al.*, "Polarimetric dehazing utilizing spatial frequency segregation of images," *Appl. Opt.*, vol. 54, no. 27, pp. 8116–8122, 2015.

[16] J. Kopf *et al.*, "Deep photo: Model-based photograph enhancement and viewing," *ACM Trans. Graph.*, vol. 27, no. 5, 2008, Art. no. 116.
[17] H. Hu, J. Wu, B. Li, Q. Guo, and J. Zheng, "An adaptive fusion algorithm for visible and infrared videos based on entropy and the cumulative distribution of gray levels," *IEEE Trans. Multimedia*, vol. 19, no. 12, pp. 2706–2719, Dec. 2017.
[18] R. Fattal, "Single image dehazing," *ACM Trans. Graph.*, vol. 27, no. 3, Aug. 2008, Art. no. 72.
[19] R. T. Tan, "Visibility in bad weather from a single image," in *Proc. CVPR*, Jun. 2008, pp. 1–8.
[20] K. He, J. Sun, and X. Tang, "Single image haze removal using dark channel prior," in *Proc. IEEE Conf. Comput. Vis. Pattern Recognit*, Miami, FL, USA, 2009, pp. 1956–1963.
[21] C. H. Yeh *et al.*, "Haze effect removal from image via haze density estimation in optical model," *Opt. Exp.*, vol. 21, no. 22, pp. 27127–27141, 2013.
[22] G. Meng *et al.*, "Efficient image dehazing with boundary constraint and contextual regularization," in *Proc. IEEE Int. Conf. Comput. Vis.*, Sydney, NSW, Australia, 2014, pp. 617–624.
[23] G. Bi *et al.*, "Image dehazing based on accurate estimation of transmission in the atmospheric scattering model," *IEEE Photon. J.*, vol. 9, no. 4, 2017, Art. no. 7802918.
[24] J. B.Wang *et al.*, "Single image dehazing with a physical model and dark channel prior," *Neurocomputing*, vol. 149, no. PB, pp. 718–728, Feb. 2015.
[25] H. M. Hu *et al.*, "Adaptive single image dehazing using joint local-global illumination adjustment," *IEEE Trans. Multimedia*, vol. 22, no. 6, pp. 1485–1495, 2019.
[26] Y. H. Lai *et al.*, "Single-image dehazing via optimal transmission map under scene priors," *J. IEEE Trans. Circuits Syst. Video Technol.*, vol. 25, no. 1, pp. 1–14, 2015.
[27] K. He, J. Sun, and X. Tang, "Guided image filtering," *IEEE Trans. Pattern Anal. Mach. Intell.*, vol. 35, no. 6, pp. 1397–1409, Jun. 2013.
[28] J. P. Tarel, "Fast visibility restoration from a single color or gray level image," in *Proc. IEEE 12th Int. Conf. Comput. Vis.*, 2010, pp. 2201–2208.
[29] G. F. Meng, Y. Wang, J. Duan, S. Xiang, and C. Pan, "Efficient image dehazing with boundary constraint and contextual regularization," in *Proc. IEEE Conf. Comput. Vis.*, Dec. 2013, pp. 617–624.
[30] Q. Zhu, J. Mai, and L. Shao, "A fast single image haze removal algorithm using color attenuation prior," *IEEE Trans. Image Process.*, vol. 24, no. 11, pp. 3522–3533, Nov. 2015.
[31] D. Berman, T. Treibitz, and S. Avidan, "Non-local image dehazing," in *Proc. IEEE Conf. Comput. Vis. Pattern Recognit.*, Jun. 2016, pp. 1674–1682.
[32] W. Wang *et al.*, "Fast image dehazing method based on linear transformation," *IEEE Trans. Multimedia*, vol. 19, no. 6, pp. 1142–1155, 2017.
[33] T. M. Bui and W. Kim, "Single image dehazing using color ellipsoid prior," *IEEE Trans. Image Process.*, vol. 27, no. 2, pp. 999–1009, Feb. 2018.
[34] J. Shin *et al.*, "Radiance–reflectance combined optimization and structure-guided l0-Norm for single image dehazing," *IEEE Trans. Multimedia*, vol. 22, no. 1, pp. 30–44, Jan. 2020.
[35] W. Wang, J. Shen, F. Guo, M. Cheng, and A. Borji, "Revisiting video saliency: A large-scale benchmark and a new model," in *Proc IEEE Conf. Comput. Vis. Pattern Recognit.*, 2018, pp. 4894–4903.
[36] W. Wang, J. Shen, and H. Ling, "A deep network solution for attention and aesthetics aware photo cropping," *IEEE Trans. Pattern Anal. Mach. Intell.*, vol. 41, no. 7, pp. 1531–1544, Jul. 2019.
[37] W. Ren *et al.*, *Single Image Dehazing Via Multi-Scale Convolutional Euralnetworks[C]//European Conference On Computer Vision*. Cham, Switzerland: Springer, pp. 154–169, 2016.
[38] B. Cai, X. Xu, K. Jia, C. Qing, and D. Tao, "DehazeNet: An end-to-end system for single image haze removal," *IEEE Trans. Image Process.*, vol. 25, no. 11, pp. 5187–5198, Nov. 2016.
[39] W. Ren, S. Liu, H. Zhang, J. Pan, X. Cao, and M.-H. Yang, "Single image dehazing via multi-scale convolutional neural networks," in *Proc. Eur. Conf. Comput. Vis.* 2016, pp. 154–169.
[40] H. Zhang, and V. Patel, "Densely connected pyramid dehazing network," in *Proc. IEEE Int. Conf. Comput. Vis. Pattern Recognit.*, 2018, pp. 3194–3203.
[41] I. Goodfellow *et al.*, "Generative adversarial nets," in *Proc. Adv. Neural Inf. Process. Syst.*, 2014, pp. 2672–2680.
[42] H. Dong *et al.*, "Multi-Scale boosted dehazing network with dense feature fusion," in *Proc. IEEE Int. Conf. Comput. Vis. Pattern Recognit.*, Seattle, WA, USA, 2020, pp. 2154–2164.
[43] A. Wang, W. Wang, J. Liu and N. Gu, "AIPNet: Image-to-image single image dehazing with atmospheric illumination prior," *IEEE Trans. Image Process.*, vol. 28, no. 1, pp. 381–393, Jan. 2018.
[44] R. Li, J. Pan, Z. Li *et al.*, "Single image dehazing via conditional generative adversarial network[C]," *Proc. IEEE Conf. Comput. Vis. Pattern Recognit.*, 2018, pp. 8202–8211.
[45] E. J. McCartney, *Optics of the Atmosphere: Scattering by Molecules and Particles*. New York, NY, USA: Wiley, 1976.
[46] B. Li *et al.*, "Reside: A benchmark for single image dehazing," *IEEE Trans. Image Process.*, vol. 28 no. 1, pp. 492–505, 2018.
[47] N. Hautière, J. P. Tarel, D. Aubert, and É. Dumont, "Blind contrast enhancement assessment by gradient ratioing at visible edges," *Image Anal. Stereol.*, vol. 27 no. 1, pp. 87–95, 2008.
[48] L. K. Choi, J. You, and A. C. Bovik, "Referenceless prediction of perceptual fog density and perceptual image defogging," *IEEE Trans. Image Process.*, vol. 24, no. 11, pp. 3888–3901, 2015.
[49] S. Zhao, L. Zhang, S. Huang, and Y. Shen, "Dehazing evaluation: Real-world benchmark datasets, criteria, and baselines," *IEEE Trans. Image Process.*, vol. 29, pp. 6947–6942, 2020.
[50] L. Zhang, Y. Shen, and H. Li, "VSI: A visual saliency-induced index for perceptual image quality assessment," *IEEE Trans. Image Process.*, vol. 23, no. 10, pp. 4270–4281, Oct. 2014.
[51] W. Xue, L. Zhang, X. Mou, and A. C. Bovik, "Gradient magnitude similarity deviation: A highly efficient perceptual image quality index," *IEEE Trans. Image Process.*, vol. 23, no. 2, pp. 684–695, Feb. 2014.
[52] L. Zhang, L. Zhang, X. Mou, and D. Zhang, "FSIM: A feature similarity index for image quality assessment," *IEEE Trans. Image Process.*, vol. 20, no. 8, pp. 2378–2386, Aug. 2011.